Tungsten and barium transport in the internal plasma of hollow cathodes

James E. Polk*, Ioannis G. Mikellides†, Ira Katz‡
Jet Propulsion Laboratory, M/S 125-109, 4800 Oak Grove Drive, Pasadena, CA 91109
Angela M. Capece§
California Institute of Technology, 1200 E. California Blvd., Pasadena, CA 91125

The effect of tungsten erosion, transport and redeposition on the operation of dispenser hollow cathodes was investigated in detailed examinations of the discharge cathode inserts from an 8200 hour and a 30,352 hour ion engine wear test. Erosion and subsequent redeposition of tungsten in the electron emission zone at the downstream end of the insert reduces the porosity of the tungsten matrix, preventing the flow of barium from the interior. This inhibits the interfacial reactions of the barium-calcium-aluminate impregnant with the tungsten in the pores. A numerical model of barium transport in the internal xenon discharge plasma shows that the barium required to reduce the work function in the emission zone can be supplied from upstream through the gas phase. Barium that flows out of the pores of the tungsten insert is rapidly ionized in the xenon discharge and pushed back to the emitter surface by the electric field and drag from the xenon ion flow. This barium ion flux is sufficient to maintain a barium surface coverage at the downstream end greater than 0.6, even if local barium production at that point is inhibited by tungsten deposits. The model also shows that the neutral barium pressure exceeds the equilibrium vapor pressure of the impregnant decomposition reaction over much of the insert length, so the reactions are suppressed. Only a small region upstream of the zone blocked by tungsten deposits is active and supplies the required barium. These results indicate that hollow cathode failure models based on barium depletion rates in vacuum dispenser cathodes are very conservative.

I. Introduction

Electric propulsion offers significant trip time and/or mass benefits for a wide range of deep space missions,[1] but the thrusters in these systems are required to operate for tens of thousands of hours to provide the required total impulses. This requirement places extraordinary demands on component reliability and makes thruster qualification difficult. Hollow cathode electron sources are key life-limiting components in these engines, and this paper describes experiments and modeling aimed at understanding cathode failures due to material transport.

State-of-the-art hollow cathodes consist of a porous tungsten tube (the insert), which is contained in a refractory metal cathode tube with an orifice plate on the downstream end. A small fraction of the thruster propellant is injected through the hollow cathode, and the orifice serves to increase the internal pressure in the insert region. Electron emission from the inner surface maintains an internal plasma which heats the insert to the required operating temperature and helps conduct the current into the main discharge. A heater surrounding the cathode is used to preheat it prior to ignition.

A low emitter operating temperature is achieved by maintaining a layer of adsorbed oxygen and barium atoms that lowers the surface work function. In state-of-the-art impregnated cathodes Ba and BaO are supplied

*Principal Engineer, Propulsion and Materials Engineering Section MS 125-109
†Member of the Technical Staff, Propulsion and Materials Engineering Section MS 125-109
‡Principal Engineer, Propulsion and Materials Engineering Section MS 125-109
§Graduate Student, California Institute of Technology

by barium calcium aluminate source material (the impregnant) incorporated in the pores of the tungsten. Gaseous Ba and BaO are released in interfacial reactions between the tungsten matrix and the impregnant, producing a temperature-dependent vapor pressure of these species inside the pores. The Ba and BaO then migrate to the surface by Knudsen flow and surface diffusion on the pore walls. In vacuum dispenser cathodes Ba adsorbates lost by evaporation are replenished by Ba and BaO through surface diffusion from the pores and most of the vapor flow from the pores is lost. In gas discharges, the vapor flow in the discharge may be transported back to the cathode surface, offering another path for replenishing Ba lost by desorption.

Near the surface, products of the impregnant reactions escape to the exterior through the pores, allowing the reactions to proceed to completion. Eventually, relatively stable tungstates are produced and production of volatile species in that region ceases. The reaction front proceeds into the insert as reactants nearer the surface are consumed and the porosity of the impregnant increases due to loss of volatile materials. The region behind the reaction front is depleted in barium and the depth of this depletion layer has been characterized in some cathode tests[2] and is an indicator of remaining useful life.

Hollow cathodes are subject to a number of potential failure mechanisms. External erosion by high energy ions created downstream of the orifice has been observed in a number of tests[3–5] and is the focus of experiments and modeling discussed elsewhere.[6,7] Damage to the emitting surface due to poisoning by reactive gases or buildup of bulk tungstate layers due to reactive impurities is another potential failure mode.[8–10]

Insert life is ultimately limited by the barium supply in the impregnant. When the barium supply rate from the interior or from the gas phase drops below the rate at which adsorbed atoms are lost from the surface by desorption, the surface coverage drops and the work function rises.[11] The cathode eventually becomes impossible to ignite or cannot be heated to the temperatures needed for the required electron current density.

Finally, tungsten transport has been observed in many extended hollow cathode tests.[3,5,11,12] Impregnated cathode temperatures are not high enough to cause significant evaporation of the tungsten matrix, so these processes are undoubtedly due to formation and subsequent dissociation of volatile tungsten compounds. No failures have been attributed to this mechanism, but it could potentially lead to cathode failure. Reduction in the cathode orifice diameter by deposition of tungsten eroded from internal surfaces could increase the operating temperature or prevent cathode ignition, and deposits of tungsten on the emitter surface may limit barium flow through the tungsten matrix.

The lack of understanding of the chemical and mass transport processes in hollow cathodes has prevented development of useful models for these failure mechanisms. This paper attempts to answer two fundamental questions as a first step to developing the required insight. First, does the erosion, transport, and deposition of tungsten in the insert region affect hollow cathode function? Second, how does gas phase transport of barium affect the operation of the cathode? These two questions turned out to be intimately linked.

The first question has been approached by a detailed examination of the cathode inserts used in several long duration ion engine wear tests. The 8200 hour Life Demonstration Test (LDT) was performed with a 30-cm engineering model thruster similar to that flown on the Deep Space 1 (DS1) mission[13,14] under the NASA Solar Electric Propulsion (SEP) Technology Applications Readiness (NSTAR) Program.[3] A subsequent Extended Life Test (ELT) was performed with the DS1 flight spare NSTAR thruster, ultimately accumulating 30,352 hours of operation at several different throttle levels.[4] Both tests were voluntarily terminated with the discharge and neutralizer cathodes exhibiting no evidence of performance degradation. The examination of these cathodes described here extends initial evaluations reported earlier[3,5] and focused specifically on material transport. The objectives were to identify erosion and deposition sites and determine if these processes modified or have the potential to impact the function of the insert as an electron emitter.

The second question was addressed by developing a model of barium transport in the gas phase. This model leverages significant work done in modeling the internal xenon gas discharge. The objectives were to study how barium enters the discharge, flows through the plasma and is redeposited on the emitter surface, and how that affects the cathode work function.

II. Experimental Characterization of Material Transport Processes

In many long-duration hollow cathode tests, restructuring of the tungsten insert and orifice plate has been observed.[3,5,11,12] This typically involves erosion in the emission zone and upstream face of the orifice plate, formation of tungsten crystals at the downstream end of the emitter, and deposition of tungsten, often in the form of large crystals, on the orifice plate and within the orifice. In some cases, films of barium compounds have been observed on the emitter surface and tungsten has been found with barium oxide in deposits between the emitter and the cathode tube.[12]

A link with reactive gases is implied by Sarver-Verhey's observation of extreme examples of these erosion and deposition phenomena in the series of cathodes that had been operated with leaky gas systems.[12] He speculated that tungsten transport was due to formation of volatile tungsten compounds which were subsequently dissociated, leaving pure tungsten deposits. The deposition of barium compounds on the emitter surface also appears to be related to the presence of oxidizing impurities.[9,10] However, the flow dynamics of barium and tungsten in the gas phase and how tungsten transport processes might affect the supply of barium from the interior of the insert are not understood. This section describes experimental findings which guided the development of the barium transport model.

II.A. Experimental Approach

The cathode inserts from the 8200 hour LDT and the 30,352 hour ELT had previously been fractured along their axes to allow inspection.[3,5] In the investigation summarized here the LDT discharge and neutralizer cathode inserts, the ELT discharge cathode insert and a control insert that had not been operated were further analyzed to gain more insight into material transport and its effect on the emission zone. The profiles of the interior surfaces were measured using a laser profilometer system with a resolution of less than 1 μm. The profilometer calibration was checked by scanning a series of steps made with precision ground ceramic blocks of different heights that had been rung onto an optical flat.

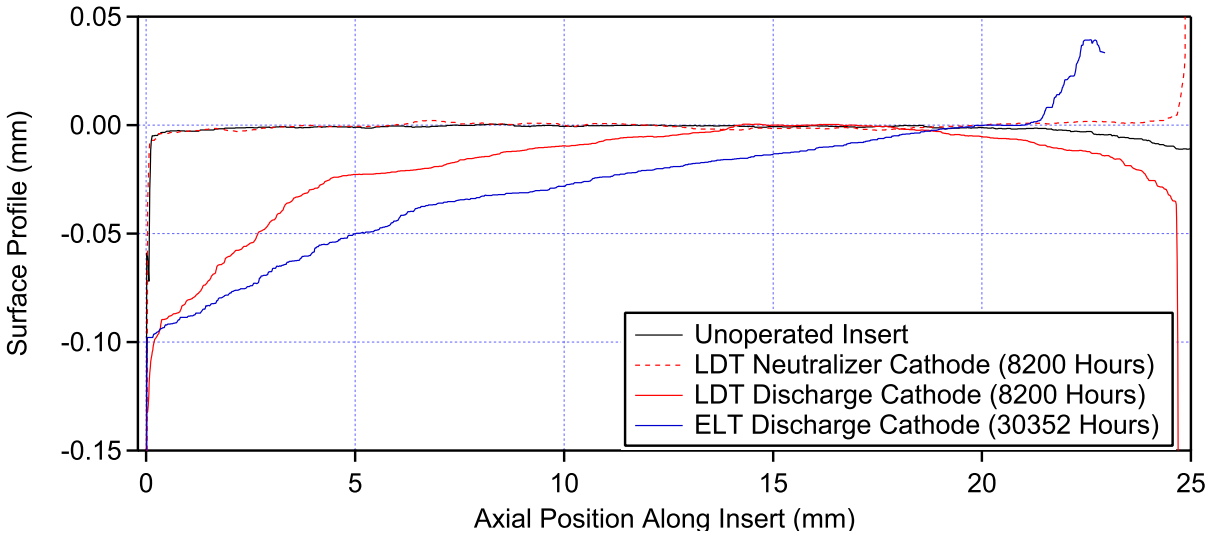

Figure 1. Axial profiles of four cathode inserts showing erosion of the interior surface.

The surface morphology and internal porosity of the inserts and the discharge cathode orifice plates were characterized in examinations with a scanning electron microscope (SEM). The composition of the impregnant and various deposits was determined using energy-dispersive spectroscopy (EDS). Several insert samples were potted to allow a fracture surface to be polished. This was done with very fine diamond abrasives wetted with kerosene to avoid removing impregnant material from the pores. SEM exams and EDS analysis were then used to characterize the the cathode bulk. In particular, element maps of the interior were created with EDS scans to reveal the distribution of impregnant material.

II.B. Erosion and Deposition Sites

The profiles of the insert inner surfaces are shown in Fig. (1). These are based on profilometer scans along the axis of the insert fragments which yielded the surface height above a flat reference plane on which the insert fragment rested. The height values were shifted so that zero height represents the original interior surface, and the erosion depth (or increase in inner radius of the cylindrical insert) is indicated by negative values. The original surface datum was clear in the control insert and the neutralizer insert, which exhibited very little internal erosion. For the discharge cathode inserts however, points near the upstream end where SEM exams showed surfaces that did not appear to be eroded or covered with deposits were assumed to be the original, uneroded surface. This is somewhat subjective, however, so the magnitude of the erosion depths indicated by negative values on the abscissa may be underestimated.

The control insert surface profile was flat to within ± 5 μm except near the upstream end where the indicated height drops slightly, which represents an increase in the insert inner radius of about 15 μm. This feature is near the interface between the porous tungsten insert and a molybdenum ring that is brazed on the upstream end, and may be an artifact of machining. The LDT neutralizer insert profile is almost identical, except that it shows a smooth, filleted transition to the molybdenum ring. The LDT discharge cathode profile exhibits erosion over 15 mm at the downstream end, with more severe erosion in the first 4-5 mm. Approximately 74 mg of tungsten was eroded from this region, which is equivalent to 4×10^{-4} moles with an average erosion rate of 1.5×10^{-9} g/cm^{2}s. The radius of this insert is also larger near the upstream end. It is not clear if this is the same kind of feature seen in the control insert, or if it indicates another erosion site.

The ELT discharge cathode insert is qualitatively similar to the LDT insert at the downstream end, although the erosion is generally deeper and the transition in the slope of the eroded surface occurs at about 7 mm from the tip. The total erosion in the ELT insert was approximately 126 mg or 6.9×10^{-4} moles with an average erosion rate of 5.2×10^{-10} g/cm^{2}s over the course of the test. Both profiles indicate a maximum eroded depth at the tip of 100 μm, which yields a peak erosion rate of 1.4–5.2×10^{-9} g/cm^{2}s. The ELT insert had thick deposits of barium compounds on the last 3 mm of the upstream end, which is seen in the profile as an increase in height of about 30-40 μm over the original surface.

Figure (2) is a composite photo constructed from SEM images of the LDT discharge cathode cross section showing the first 5 mm of the downstream end. The upper surface is the interior of the cylindrical insert, and the white line indicates the original surface, highlighting the erosion in the emission zone. The insert manufacturing process includes a weak etch after impregnation to remove impregnant from the surface and pores near the surface. This prevents excess barium production early in cathode operation. The surface layer from which the impregnant has been removed is apparent in the photo as a region with dark pores. The porosity of the tungsten matrix is actually very uniform throughout the insert, but in this region the pores are emphasized because they are filled with potting material, which looks dark in the secondary electron imaging mode. The impregnant-free layer has been removed from the emitting zone by erosion.

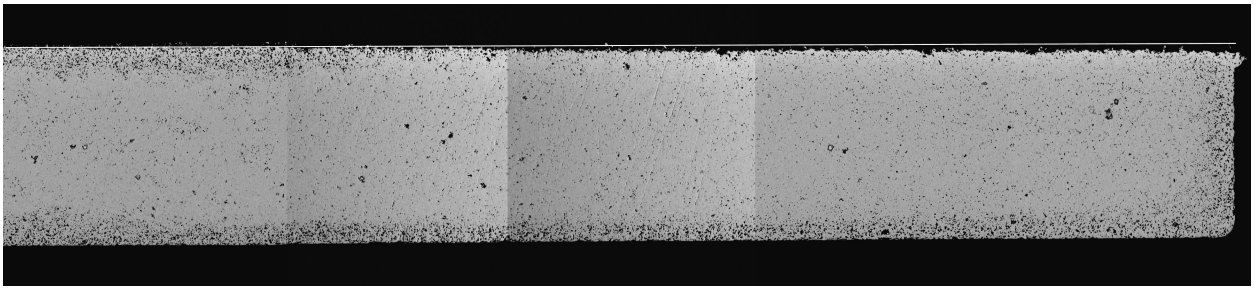

Figure 2. Cross section of the cathode insert showing erosion on the downstream end.

Figures (3) through (6) summarize SEM exams of the inner insert surface morphology. The morphology of the control insert does not vary over the inner surface. On this scale a large number of pores with a diameter of 1- 5 μm are visible as shown in Fig. (3).

The morphology of the ELT discharge cathode insert varies considerably with position, as shown in Fig. (4). Photomicrographs A and B show tungsten crystals that were noted earlier[5] and have been observed in

many long duration tests.[3,11,12] What is most striking about these photomicrographs is that they reveal a dramatic restructuring of the surface. This is evidently not only a site of erosion, but also of subsequent redoposition, resulting a net recession of the surface accompanied by densification of the matrix. In this region the surface porosity is much lower than the original surface. Image C represents a transition from the region with crystalline deposits to the original porous structure. Image D shows that by 10 mm from the downstream end the surface looks very similar to that of the unoperated insert, although the profile data indicate that net erosion has occurred here. With the exception of the thick barium deposits found on the upstream end of the insert, very little barium was observed on the emitter surface.

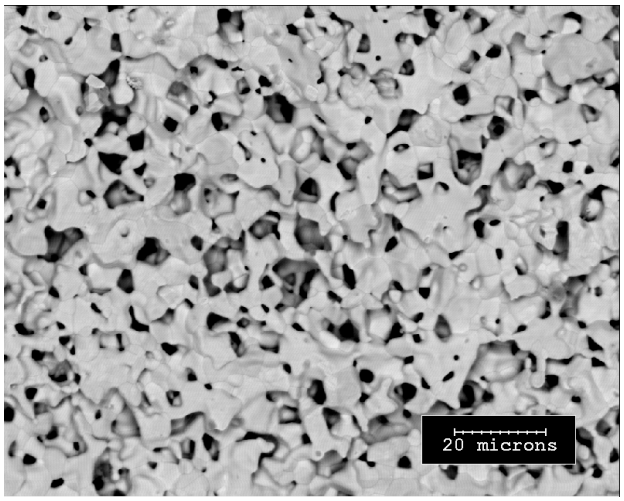

Figure 3. SEM image of the control insert inner surface.

Six distinct zones found along the axis of the LDT insert are identified in Fig. (5). A region about 2 mm long at the downstream end of the insert tube was densely covered with fine tungsten crystals and a less dense covering of much larger crystals, as shown in the photomicrograph in Fig. (6). This image is at a lower magnification but is qualitatively similar to those from the ELT, showing the formation of a dense tungsten layer by some combination of erosion and redeposition at the downstream end. This coating also appeared to significantly reduce the porosity of the surface in this region. Some areas with barium deposits were found in this zone.

A 2 mm region upstream of the first zone was also covered with the small crystals and some large ones, but had very little barium on the surface. A third region about 1.7 mm long upstream of that had a surface similar to a new sintered insert with some of the smaller crystals. This region also had some barium deposits in the matrix. A region about 5.3 mm long in the center of the insert tube was composed of a sintered porous tungsten matrix with very little evidence of barium. The surface of a fifth region about 3.7 mm long near the upstream end of the insert was almost completely covered with a coating containing barium, calcium, aluminum and oxygen–presumably the original impregnate material. The upstream end of the tube was primarily the tungsten matrix with isolated patches of barium, calcium, aluminum and oxygen in the pores.

II.C. Impact on Barium Transport

A significant effort was made to determine the distribution of impregnate materials to help understand barium depletion and transport. Because the impregnant is found primarily in the pores, measurements of the distribution of the impregnant species Ba, Ca, Al and O at small scales tend to be dominated by local fluctuations between the pores and the tungsten matrix. EDS line scans along fracture or cross section surfaces are generally too noisy to extract meaningful information on the distribution of barium-containing materials beneath the surface. In this case we were successful in visualizing the distribution in the interior of the LDT discharge cathode with EDS element maps and in reconstructing element profiles with depth by integrating map data over relatively wide lateral swaths to average out fluctuations in signal intensity due to local nonuniformities in density.

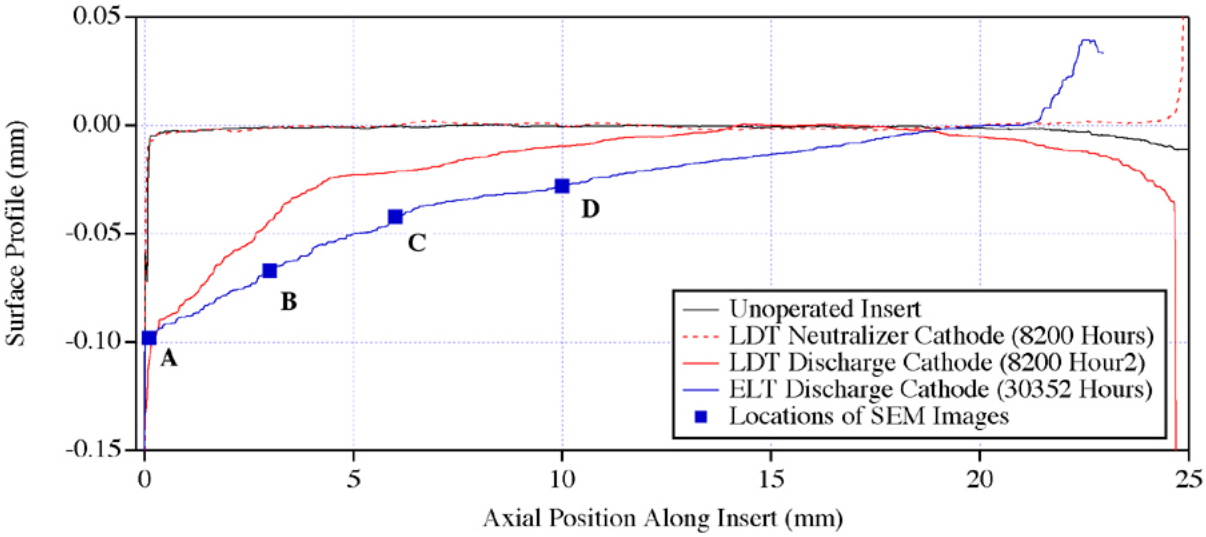

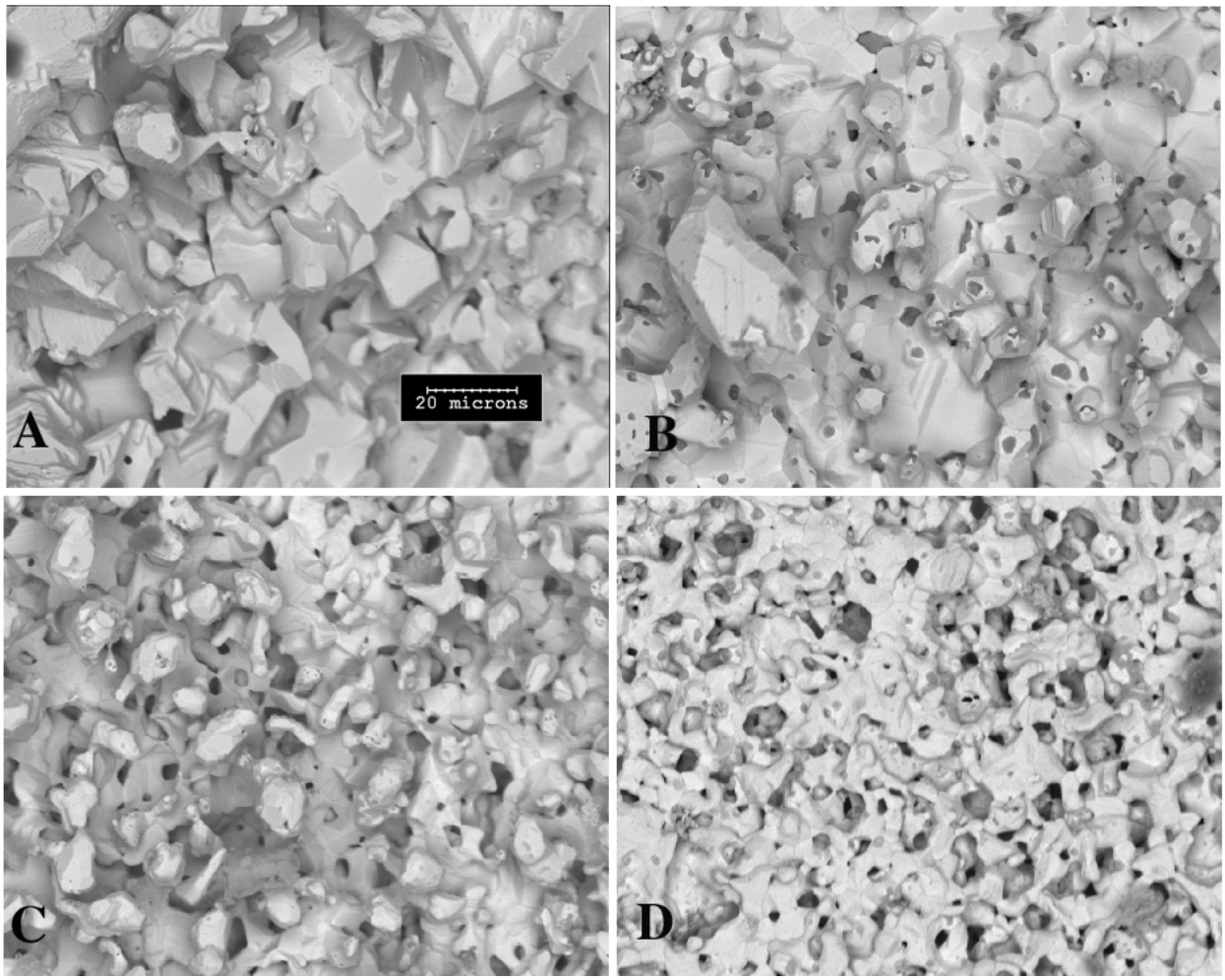

Figure 4. SEM images of the ELT discharge cathode insert inner surface.

Figure 5. Six zones on the interior of the discharge cathode insert.

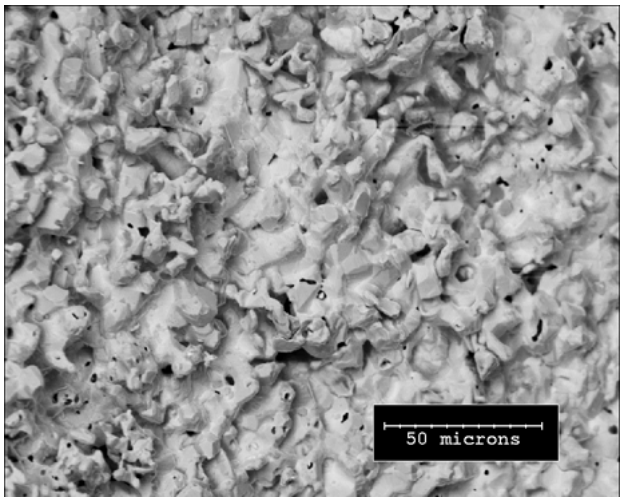

Figure 6. SEM image of the LDT discharge cathode insert inner surface near the downstream end.

Figure (7) shows the barium element map for the cathode cross section pictured in Fig. (2). As expected,

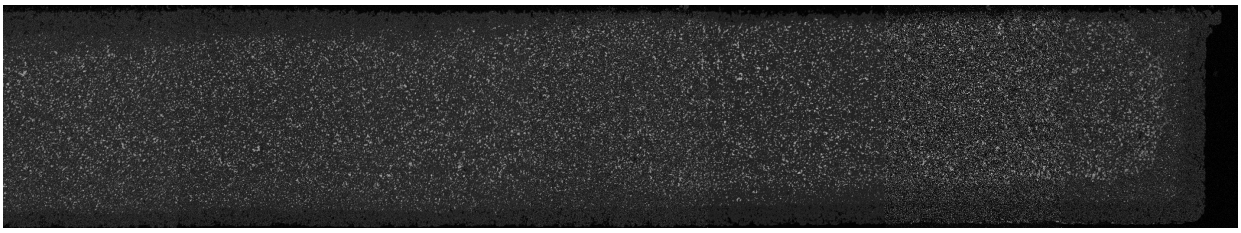

Figure 7. Cross section of the LDT discharge cathode insert showing the concentration of barium.

the image is dark in the potting material around the insert and in the impregnant-free surface layer noted in Fig. (2). The signal intensity is highest deep in the interior, where there is unreacted impregnant. The important feature in this image is the region with an intermediate signal strength. This zone is found in the upper left, under the impregnant-free layer, in the upper right corner, the downstream face on the right side and along the bottom of the insert between the impregnant-free layer and the unreacted impregnant. However, this zone is not visible under the eroded zone in the upper right. Here the brightest zone extends nearly to the surface.

This is shown quantitatively in Fig. (8). The image is a barium element map of a region on the cross-sectioned LDT discharge cathode insert approximately 0.8 mm long located just upstream of the tip. The right side is the the electron emission zone on the inner diameter of the insert and the left side is the outer diameter of the insert. The bright points are concentrations of barium in the tungsten matrix. The tungsten shows as a faint background in this image.

The barium-free zone where the insert was etched after impregnation is faintly visible on the left side, but has been mostly removed by erosion on the right. The yellow line is the sum of the columns composing the image and represents the average barium signal strength at each radial location. This analysis method eliminates much of the noise that would be associated with a line scan across the sample. The white trace is based on a similar analysis of the calcium element map. The tungsten background has been subtracted from these signals. On the left side of the image is an intermediate layer where the barium signal drops to about half the value in the interior and the calcium signal drops nearly to zero. This is the zone from which impregnant material has been depleted by reactions with the tungsten. The space between the insert and the cathode tube was filled with a layer of barium oxide, which is undoubtedly the result of reaction products flowing out from this reaction zone. On the right side of the image a thin region with little or no impregnant is visible, but there is no depletion layer as on the left. The barium and calcium signals are uniform up to the tungsten layer. Upstream of the region with the heaviest erosion the depletion layer can be found on both surfaces of the cathode, although the layer thickness decreases with increasing distance upstream.

The picture that emerges from these data is that material is eroded from the insert, particularly in the emission site at the downstream end, but some fraction of it is redeposited locally. The local redeposition in the emission zone forms a much denser tungsten shell that apparently impedes the flow of barium from the interior, inhibiting the reduction of the impregnate material under the emission zone. Barium lost from the emitter by evaporation in this zone must be replenished through the gas phase by barium released further upstream.

Further evidence for this was obtained in an experiment performed on Qinetiq T6 ion engine discharge cathodes.[15] To simulate heavily depleted emitters, several special two-piece inserts were fabricated in which the upstream segment was a conventional impregnated porous tungsten tube and the downstream porous tungsten segment (either 25 or 50% of the total length) was not impregnated. Cathodes with these inserts ignited easily and appeared to operate just like cathodes with normal inserts. This strongly suggests that the downstream portion of the emitter can be supplied with barium through the gas phase.

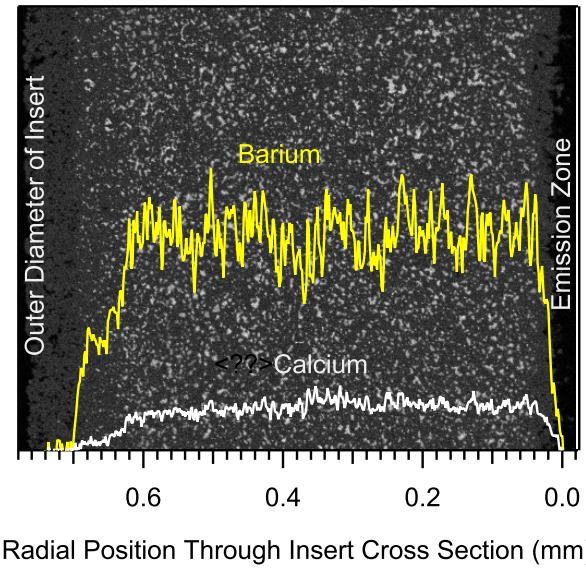

Figure 8. Barium element map and profiles for barium and calcium in a cross section of the LDT cathode.

III. Barium Transport in the Hollow Cathode Internal Plasma

The purpose of this model is to understand barium transport in the xenon plasma and in particular how the cathode operates when a dense tungsten deposit on the downstream end prevents barium flow from the interior of the insert. The initial focus is on barium because this is the dominant species produced by the insert,[16] although the model will be extended to include BaO flow and chemistry. Barium transport is strongly influenced by the xenon plasma; the electron density and temperature control the ionization of barium, the electric field in the xenon plasma and collisions with Xe and Xe ions control the diffusion of barium. However, barium atom and ion densities are so low they do not significantly modify the charge density or temperature in what is primarily a xenon discharge. This allows us to separate the problem into two parts, and use the major species parameters predicted by a xenon discharge model as fixed quantities in the solution of the minor species transport equations.

III.A. Minor Species Transport Equations

The momentum equation for species i can be written

$$\begin{aligned}&\frac{\partial(n_i m_i \mathbf{u}_i)}{\partial t} + \nabla \cdot (n_i m_i \mathbf{u}_i \mathbf{u}_i) = \\ &-\nabla P_i - \nabla \cdot \tau_i + m_i(S_i \mathbf{u}_{i,birth} - R_i \mathbf{u}_{i,death}) \\ &+n_i q_i(\mathbf{E} + \mathbf{u}_i \times \mathbf{B}) + \sum_j n_i \nu_{ij} \mu_{ij}(\mathbf{u}_i - \mathbf{u}_j)\end{aligned} \tag{1}$$

where n_i is the density of species i, m_i is the mass, $\mathbf{u}_i$ is the velocity, P_i is the partial pressure, τ_i is the viscous stress tensor, S_i is the rate at which species i particles are created (by ionization reactions, for instance), $\mathbf{u}_{i,birth}$ is the average velocity of newly created i particles, R_i is the rate at which i particles are lost (through recombination, for example) and $\mathbf{u}_{i,death}$ is the mean velocity when they are lost, q_i is the particle charge, and $\mathbf{E}$ is the electric field and $\mathbf{B}$ is the magnetic field. The final term represents momentum lost from species i in collisions with species j, which is proportional to the collision frequency ν_{ij}, the reduced mass μ_{ij} and the mean relative velocity between the populations. The species continuity equation is

$$m_i \frac{\partial n_i}{\partial t} + m_i \nabla \cdot (n_i \mathbf{u}_i) = m_i(S_i - R_i) = m_i \dot{n}_i, \tag{2}$$

where $\dot{n}_i$ is the net rate at which species i is created.

Expanding the derivatives in the momentum equation reveals terms identical to the left-hand side of the continuity equation multiplied by the species velocity. The terms on the right-hand side of the momentum equation that are associated with particle creation and loss are identical the right-hand side of the continuity equation multiplied by the mean species velocity, if we assume $\mathbf{u}_{i,birth} = \mathbf{u}_{i,death} = \mathbf{u}_i$. These terms can therefore be subtracted out. If we neglect the viscous term and magnetic field effects, the momentum equation simplifies to

$$\begin{aligned} &n_i m_i \frac{\partial \mathbf{u}_i}{\partial t} + n_i m_i \mathbf{u}_i \cdot \nabla \mathbf{u}_i = \\ &-\nabla P_i + n_i q_i \mathbf{E} + \sum_j n_i \nu_{ij} \mu_{ij} (\mathbf{u}_j - \mathbf{u}_i) \end{aligned} \tag{3}$$

If the phenomena of interest are sufficiently slow, i.e. there are no high frequency phenomena and fluid acceleration is small compared to the force terms, we may neglect the momentum terms on the left-hand side and the resulting equation can be solved for the species flux, $\mathbf{\Gamma}_i = n_i \mathbf{u}_i$. For example, if we write Eq. (3) for barium ions (Ba^+) including momentum transfer collisions with electrons (e), xenon ions (Xe^+) and xenon neutrals (Xe), we obtain

$$\begin{aligned} 0 \quad &= -\nabla P_{Ba^+} + e n_{Ba^+} \mathbf{E} \\ &- n_{Ba^+} [\nu_{Ba^+ e} \mu_{eBa} (\mathbf{u}_{Ba^+} - \mathbf{u}_e) \\ &+ \nu_{Ba^+ Xe^+} \mu_{BaXe} (\mathbf{u}_{Ba^+} - \mathbf{u}_{Xe^+}) \\ &+ \nu_{Ba^+ Xe} \mu_{BaXe} (\mathbf{u}_{Ba^+} - \mathbf{u}_{Xe})] \end{aligned} \tag{4}$$

Collisions between barium ions and other minor species (such as Ba and BaO) are assumed to be sufficiently rare to neglect. Recognizing that $\mathbf{u}_e \gg \mathbf{u}_{Ba^+}$, that $\mathbf{u}_{Xe}$ is negligible, and that $\mu_{eBa} \simeq m_e$, we obtain

$$\begin{aligned} 0 \quad &= -\nabla P_{Ba^+} + e n_{Ba^+} \mathbf{E} \\ &- n_{Ba^+} [-\nu_{Ba^+ e} m_e \mathbf{u}_e \\ &+ \nu_{Ba^+ Xe^+} \mu_{BaXe} (\mathbf{u}_{Ba^+} - \mathbf{u}_{Xe^+}) \\ &+ \nu_{Ba^+ Xe} \mu_{BaXe} \mathbf{u}_{Ba^+}] \end{aligned} \tag{5}$$

Solving this equation for the barium ion flux yields

$$\begin{aligned} \mathbf{\Gamma}_{Ba^+} \quad &= n_{Ba^+} \mathbf{u}_{Ba^+} = \\ &\frac{-\nabla P_{Ba^+} + e n_{Ba^+} \mathbf{E}}{\nu_{Ba^+ Xe^+} \mu_{BaXe} (1 + \nu_{Ba^+ Xe} / \nu_{Ba^+ Xe^+})} \\ &+ n_{Ba^+} \left(\frac{\nu_{Ba^+ e} / \nu_{Ba^+ Xe^+}}{1 + \nu_{Ba^+ Xe} / \nu_{Ba^+ Xe^+}} \right) \left(\frac{m_e}{\mu_{BaXe}} \right) \mathbf{u}_e \\ &+ n_{Ba^+} \left(\frac{1}{1 + \nu_{Ba^+ Xe} / \nu_{Ba^+ Xe^+}} \right) \mathbf{u}_{Xe^+} \end{aligned} \tag{6}$$

The first term represent ion flux driven by pressure gradient and electrostatic forces. The second and third terms are the fluxes driven by drag due to collisions with electrons and xenon ions, respectively. The collision frequency terms are cast in the form of ratios to the dominant interaction, coulomb collisions between xenon and barium ions. The electron drag term can be neglected because of the small electron-to-heavy particle mass ratio.

The same approach yields the flux of neutral barium atoms,

$$\begin{aligned} \mathbf{\Gamma}_{Ba} \quad &= n_{Ba} \mathbf{u}_{Ba} = \frac{-\nabla P_{Ba}}{\nu_{BaXe} \mu_{BaXe} (1 + \nu_{BaXe^+} / \nu_{BaXe})} \\ &+ n_{Ba} \left(\frac{\nu_{BaXe^+} / \nu_{BaXe}}{1 + \nu_{BaXe^+} / \nu_{BaXe}} \right) \mathbf{u}_{Xe^+} \end{aligned} \tag{7}$$

Electron drag has also been neglected in this equation.

The ion-ion collision frequency that appears in these equations is given by the standard coulomb frequency,

$$\nu_{Ba^+Xe^+} = \frac{\sqrt{2}}{3\sqrt{\pi}} n_{Xe+} \left(\frac{e^2}{4\pi\epsilon_0}\right)^2 \frac{4\pi}{m_{Ba}^{1/2}(kT_h)^{3/2}} \times \left(\frac{m_{Xe}}{m_{Ba}+m_{Xe}}\right)^{1/2} \ln\Lambda_i \tag{8}$$

The neutral barium-xenon collision frequency is expressed in terms of a constant scattering cross-section $\sigma_D = 40\text{Å}^2$ based on diffusion measurements for barium in xenon.[17]

$$\nu_{BaXe} = n_{Xe}\sigma_D \left(\frac{8kT_h}{\pi\mu_{BaXe}}\right)^{1/2} \tag{9}$$

Ba ion-Xe neutral and Ba neutral-Xe ion collisions are assumed to have same cross section.

The continuity equations for barium ions and neutrals can be expressed in terms of the fluxes,

$$\frac{\partial n_{Ba^+}}{\partial t} + \nabla\cdot\mathbf{\Gamma}_{Ba^+} = \dot{n}_{Ba^+} \tag{10}$$

$$\frac{\partial n_{Ba}}{\partial t} + \nabla\cdot\mathbf{\Gamma}_{Ba} = \dot{n}_{Ba} = -\dot{n}_{Ba^+} \tag{11}$$

where $\dot{n}_{Ba^+}$ is the rate at which barium ions are created by ionization of barium neutrals and $\dot{n}_{Ba}$ is the rate at which neutrals are consumed by ionization reactions. The ionization rate is given by the product of the barium atom density and the ionization rate coefficient, $\dot{n}_{Ba^+}(Te) = n_{Ba}\nu_{Ba}^{iz}$. The ionization rate coefficient for Ba was obtained by integrating measured barium ionization cross sections[18] over a Maxwellian velocity distribution,

$$\nu_{Ba}^{iz} = n_e < \sigma_i \mathbf{u}_e > . \tag{12}$$

The model also employs the ideal gas equation of state. The barium ions and neutrals are assumed to equilibrate with the xenon atoms and ions, so all heavy particles have a single temperature T_h.

III.B. Boundary Conditions

The continuity equations are solved on a 2D axisymmetric region two cm long encompassing the insert plasma at the downstream end of the emitter. The simulation domain is bounded by 5 surfaces as shown in Fig. (9), including the centerline, the entrance to the cathode orifice, the upstream face of the orifice plate, the emitter surface and the upstream inlet to the cathode. Ion and neutral fluxes through these surfaces are specified as boundary conditions.

Centerline. The centerline is a symmetry boundary, so the ion and neutral fluxes are set equal to zero.

Emitter Surface. The source of barium is flow from the interior through the porous tungsten structure (and reaction products in the pores), and the rate at which barium is dispensed depends on three main parameters: insert temperature, barium partial pressure in the insert plasma and time. The impregnant decomposition reaction is assumed to be strongly diffusion-limited, so the barium pressure at the reaction front is very close to the equilibrium pressure of barium over the reactants, which is a function of the insert temperature. The diffusive flow or knudsen flow through the pores and reaction products in the insert is driven by the difference in the pressure at the reaction front and the barium partial pressure at the insert surface. Finally, the reaction front recedes into the insert as the barium is consumed, so the flow resistance increases with time.

Measurements[2] of the barium supply rate from S-type cathodes in vacuum early in life (with a total operating time t_{ref} on the order of 10 hours) are used to define the maximum supply rate Γ_s^{max} in atoms/cm^{2}s as a function of cathode temperature T_c in K.

$$\ln\Gamma_s^{max}(T_c, P_{Ba}=0, t_{ref}) = 63.53 - 46237/T_c \tag{13}$$

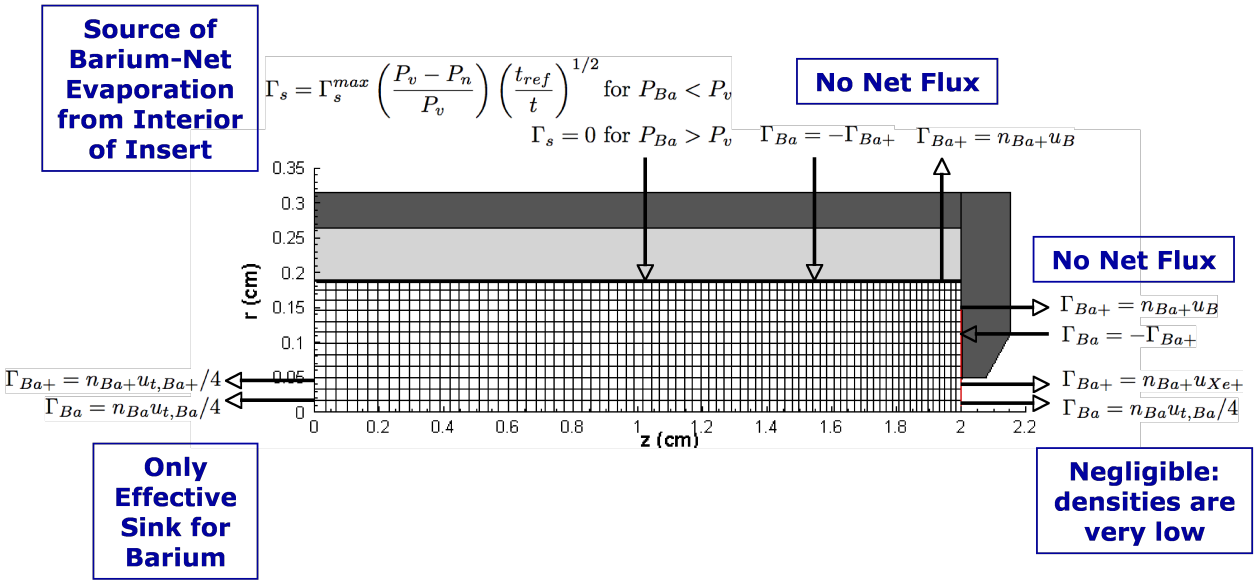

Figure 9. Boundary conditions and computational grid for the barium transport model.

The temperature distribution measured along the axis of an emitter at the NSTAR full power operating condition shown in Fig. (10) is used in all of the simulations to calculate the maximum barium flow rate as a function of position.

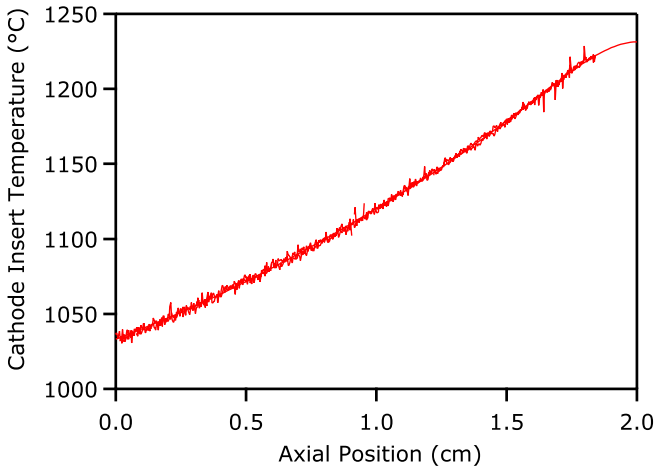

Figure 10. Axial temperature distribution along the insert inner surface.

The calculated barium partial pressure in the insert is used to determine the reduction in barium flow, assuming an equilibrium pressure P_v in Torr for the impregnant decomposition reaction proposed by Rittner,[19]

$$\log P_v = 8.56 - 20360/T_c \tag{14}$$

In cases for which the ambient barium pressure exceeds the equilibrium pressure, the reaction is assumed to cease. The barium supply rate has been observed to decrease as $t^{-1/2}$ for time t, which is consistent with Knudsen flow through a flow resistance which increases as barium is lost and the reaction front recedes into the surface.[19,20] The net barium flow can then be expressed as

$$\Gamma_e(T_c, P_{Ba}, t) = \Gamma_e(T_c, P_{Ba} = 0, t = t_{ref}) \times \left(\frac{P_v - B_{Ba}}{P_v}\right)\left(\frac{t_{ref}}{t}\right)^{1/2}. \tag{15}$$

Ba neutrals and ions also flow back to the insert surface. However, the cathode temperatures are too high for barium to accumulate in thick layers on the surface (the evaporation rate for bulk barium at these temperatures exceeds the ion and neutral fluxes by many orders of magnitude), so we assume that the surface has a steady state, submonolayer coverage of barium adsorbed on oxygen on tungsten. In steady state, there is no net total barium flux to the surface. The neutral flux to the surface is balanced by the desorption of neutrals, and ions that strike the surface return to the plasma as neutral barium atoms, so there is a net neutral flow (in addition to the neutral flow from insert interior) which is equal in magnitude to the ion flow. This assumption is consistent with the observations from the ELT that barium does not accumulate on the downstream surfaces of the inserts.

Orifice Plate Upstream Face. This surface was also assumed to have a steady-state, submonolayer coverage with a net neutral flow from the surface equal to the impinging ion flux.

Entrance to Cathode Orifice. Neutrals were assumed to flow out of the cathode orifice with their thermal velocity. Ions were assumed to have the same velocity at this point as the xenon ions. In practice, there are very few barium ions or neutrals in this region, so the results are not sensitive to these assumptions.

Upstream Boundary. The upstream boundary is the only major sink for barium. Ions and neutrals were assumed to flow out this surface with their thermal velocities and condense on cooler surfaces upstream, as observed experimentally.[3,5]

III.C. The Background Xenon Plasma Solution

The barium transport model depends on a number of xenon plasma parameters, including the xenon ion and atom densities and heavy particle temperature, which appear in the collision frequencies, the electron density and temperature, which determine the barium ionization rate, and the xenon ion velocity and electric field, which appear in the force terms of the momentum equations. These quantities are taken from a separate simulation of the xenon plasma and are assumed to be independent of the dynamics of the barium plasma.

The internal xenon plasma and neutral gas are modeled with eight governing equations which represent species continuity, momentum and energy conservation. The equations are described in detail elsewhere[21] and will only be summarized here. Continuity and momentum equations similar to Eqs. (2) and (3) are solved for xenon ions, xenon atoms and electrons. The inertia terms are neglected in both the electron and ion momentum equations. The neutral atom bulk velocity is assumed to be negligible compared to the ion and electron bulk velocities, so the neutral gas dynamics are neglected. The functional forms of the collision frequencies and ionization rates are similar to those described above. Although previous work has suggested that the classical resistivity may be enhanced anomalously by streaming instabilities downstream of the orifice entrance,[22] only classical resistivity has been used in the present simulations. The comparisons with the measurements in this cathode suggest that classical resistivity is sufficient to characterize the plasma inside the emitter region. The system includes an electron energy equation that includes energy input from the electric field, convection, conduction and energy transfer to the heavy species. It is assumed that ions and neutrals are in thermal equilibrium, so a single energy conservation equation which includes convection, conduction and heat transfer from electrons is derived for the heavy species.

These equations yield the steady-state profiles of the following variables: plasma particle density $n_{Xe^+} = n_e$, ion and electron current densities $\mathbf{j}_i$ and $\mathbf{j}_e$, respectively, electron temperature T_e, electric field $\mathbf{E}$, plasma potential ϕ, neutral particle density n_{Xe}, and heavy species temperature T_h. The total pressure P is assumed to be uniform throughout the cathode channel and the neutral particle density is determined using the ideal gas law.

A mixture of flux and Dirichlet boundary conditions are used, depending on the quantity and the boundary. The electron flux from the insert boundary is given by thermionic emission at a specified cathode temperature according to the Richardson equation with a reduction in the work function due to the Schottky effect and an effective increase in emitting area due to surface morphology.[23] Electrons with sufficient energy are allowed to flow from the plasma into conducting walls. Ions are assumed to flow into conducting surfaces with a flux $\Gamma_{Xe+} = 0.6 n_{Xe^+} u_B$, where $u_B = \sqrt{kT_e/m_{Xe}}$ is the Bohm velocity and the factor 0.6 accounts for acceleration of ions in the presheath. Ions are assumed to flow out of the upstream boundary at their

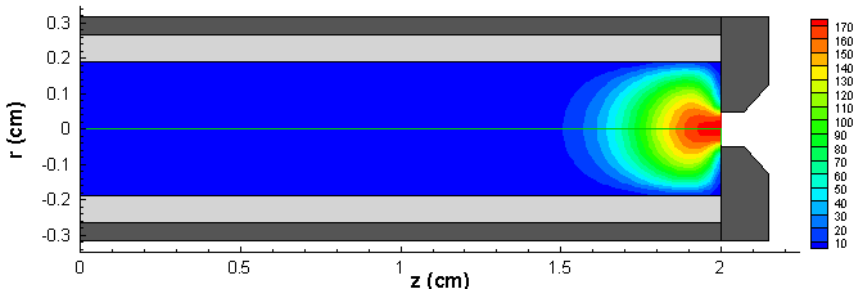

(a) Electron Density, $n_e/10^{19}$ (m^{-3})

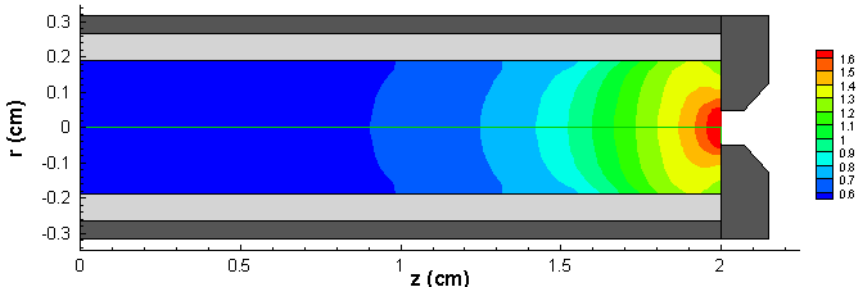

(b) Electron Temperature, T_e (eV)

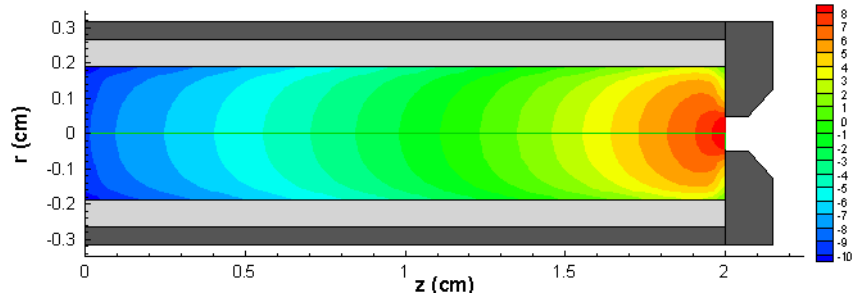

(c) Plasma Potential, ϕ (V)

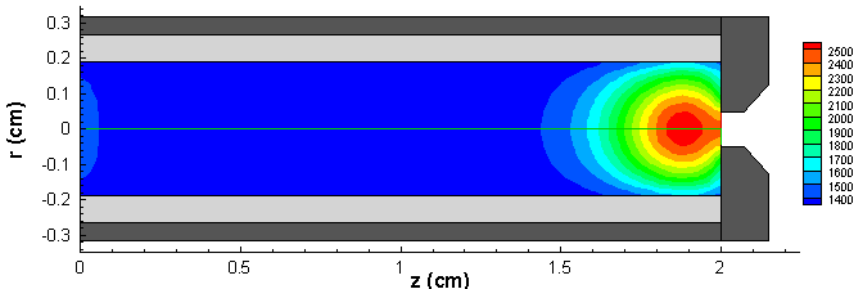

(d) Heavy Particle Temperature, T_h (K)

Figure 11. Distributions of key plasma parameters in the hollow cathode interior based on the xenon plasma model.

thermal velocity. Gas temperatures are set equal to the walls and adiabatic conditions are enforced at the cathode inlet and orifice entrance. Electron heat transfer into material surfaces is set equal to zero while electrons absorbed from the plasma convect thermal energy and potential energy associated with the work function. The plasma density and potential on the centerline at the orifice entrance are specified and the potential of all conducting surfaces is set equal to zero (ground).

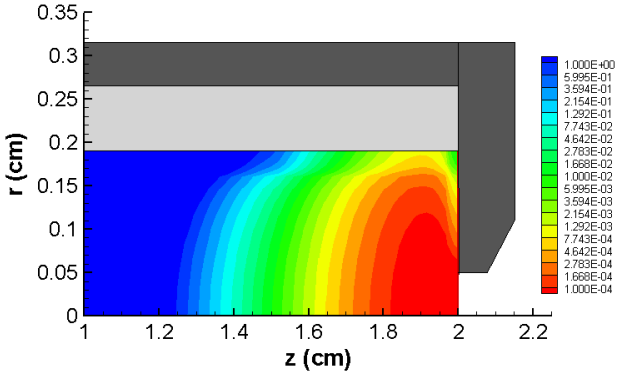

Figure 12. Mean free path for barium ionization, λ_{mfp}^{iz}, (m).

The conservation equations are discretized using finite volumes and solved on the computational mesh shown in Fig. (9). The flux vectors are edge-centered and the scalar variables are cell-centered. The fluxes are determined using second-order accurate finite differences. The system of equations is solved in a time-split manner using explicit timemarching for the plasma particle density and electron temperature. Initial estimates of the electron current density vector field, plasma particle density and electron temperature are used to compute all required fluxes, transport coefficients and related quantities. The ion continuity and electron energy equations are then time-marched to yield new values of n_e and T_e. The evolution of these equations at fixed current density is repeated for N iterations. When N reaches a specified value, conservation of total current is solved implicitly to determine a new value of the plasma potential, which is in turn used to compute the new electric field $\mathbf{E}$. The electron current density vector field is then updated using the electron momentum equation. Concurrently, the heavy species energy equation is solved implicitly to determine the new heavy species temperature T_e. The procedure is repeated until the solution for all quantities has reached steady state. The five main inputs to the numerical model are the total discharge current, the internal cathode pressure P, the plasma density at the orifice boundary, the plasma potential at the orifice boundary, and the emitter temperature as a function of position. In the simulations the orifice plasma density has been specified based on measurements, and the plasma potential at the orifice boundary is varied by iteration until the required discharge current is obtained.

The results of a simulation of the NSTAR full power point at a discharge current of 13.3 A and a xenon flow rate of 3.7 sccm are plotted in Fig. (11). Electron emission is concentrated at the downstream end of the emitter, producing a strong peak in plasma density. The high current density in the orifice results in a peak in the electron temperature on the centerline at the orifice entrance. The plasma potential is also peaked at the orifice, and drops radially and axially. The heavy particle temperature peak where the plasma density and electron temperature are highest. These distributions were used for all barium transport simulations reported in the next section.

The mean free path for barium atom ionization $\lambda_{mfp}^{iz} = u_{t,Ba}/\nu_{Ba}^{iz}$ based on the barium atom thermal velocity $u_{t,Ba} = (8kT_h/\pi m_{Ba})^{1/2}$ and the ionization frequency was calculated using the electron density and temperature profiles and is plotted in Fig. (12). The mean free path for ionization upstream of the dense plasma region is on the order of meters, but drops to 0.1 mm near the orifice. Barium atoms that drift into the dense xenon plasma have a high probability of being ionized.

III.D. Barium Transport Solutions

The xenon plasma code was modified to solve a discretized form of Eqs. (10) on the same computational domain and mesh shown in Fig. (9). The barium ion and neutral densities were initially assumed to be a uniform low value, and the continuity equations were then time-marched until the densities and fluxes achieved steady state values. Two cases were simulated. In the first case, the entire insert surface was allowed to emit barium, except where the neutral barium pressure exceeded the equilibrium vapor pressure for the reaction. In the second case, the barium supply from four mm at the downstream end of the insert was set to zero to simulate the effect of pore closure by tungsten deposits. In both cases the accumulated operating time was assumed to be 1000 hours, so the barium supply rate was a factor of 10 times lower than the beginning-of-life values from[2] due to recession of the reaction front.

The neutral and ion density distributions for the two cases are plotted in Fig. (13). In both cases the distributions are qualitatively similar. Figures (13a) and (13c) show that the neutral density peaks near the emitter surface at about 1.4 cm. This occurs because the emitter is the main source of barium neutrals. However, the neutral density drops to a very low value in a hemispherical region centered on the cathode orifice. Comparison with Fig. (12) reveals that this corresponds to the location in the discharge where the barium ionization mean free path is small. Barium neutrals emitted by the insert are consumed in ionization collisions when they enter the intense xenon plasma, and Figures (13b) and (13d) demonstrate that the resulting ion distribution peaks in a thin ionization front at the periphery of the xenon discharge zone.

The streamlines plotted in Figures (13a) and (13c) represent the net flow of barium, i.e. the sum of the barium ion and neutral fluxes, in the insert plasma. As expected, neutrals supplied by the insert or generated by neutralization of ions striking the conducting boundaries ultimately flow upstream to the sink on the upstream boundary. The diffusive flux upstream of the 1 cm location is driven primarily by the density gradient. As the barium flow from the insert increases, the peak neutral density rises to produce a density gradient and efflux sufficient to balance the influx. The dynamics at the downstream end are more complex.

Figure (14) shows the ion density distributions with vectors that represent the ion fluxes. The ion fluxes are primarily in the positive r-direction, reflecting the fact that the electrostatic and xenon ion drag forces exceed the barium ion pressure gradient force by about one order of magnitude. The ion flux to the emitter peaks at the downstream end, even in case 2, in which barium flow from the insert is inhibited to model the effect of tungsten deposits.

The calculated neutral barium partial pressure near the emitter is compared to the equilibrium barium pressure over the reaction zone in Fig. (15). In both cases the equilibrium vapor pressure profile follows the cathode temperature profile, increasing monotonically in the downstream direction. The axial neutral pressure distribution first rises in the downstream direction, then drops where the electron density and temperature peak, due to ionization. The neutral pressure rises again near the orifice plate in a small recirculation zone that is generated in the corner. The ambient barium pressure exceeds the equilibrium vapor pressure over most of the insert length, suppressing the reactions in the interior of the porous tungsten dispenser. In case 1, barium is supplied from a region only about 2.5 mm long at the downstream end of the insert. In case 2, barium emission in this zone is inhibited, but the neutral pressure is lower by about a factor of four, so a small region just upstream of this zone can supply barium (at a rate about four times lower than that in case 1).

The axial distribution of the barium ion flux to the emitter is plotted in Fig. (16). For case 1, the ion flux peaks at the downstream end and has a maximum value of 5×10^{18} $m^{-2}s^{-1}$. For case 2, the ion flux distribution is broader and the peak value is about an order of magnitude lower.

III.E. Surface Coverage of Barium Due to Transport in the Gas Phase

The barium surface coverage that can be maintained with barium resupply from the gas phase can be estimated using a surface kinetics model. If we neglect the contribution from surface diffusion out of the pores in the tungsten and assume there are no weakly bound precursor states for adsorbed barium, the time

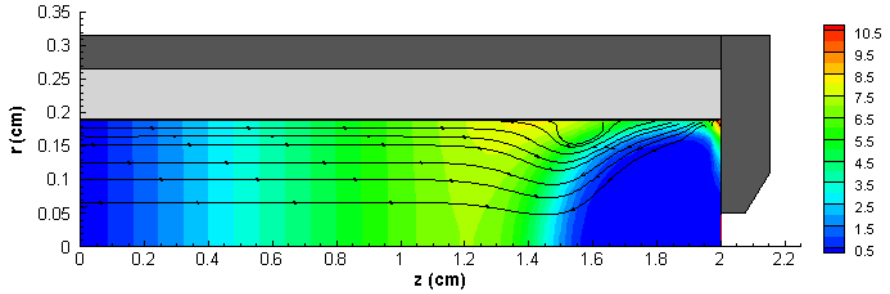

(a) Barium neutral density, $n_{Ba}/10^{16}$ (m^{-3}), for Case 1

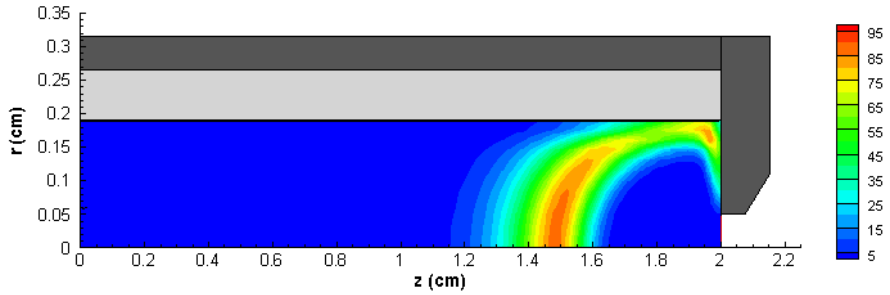

(b) Barium ion density, $n_{Ba+}/10^{14}$ (m^{-3}), for Case 1

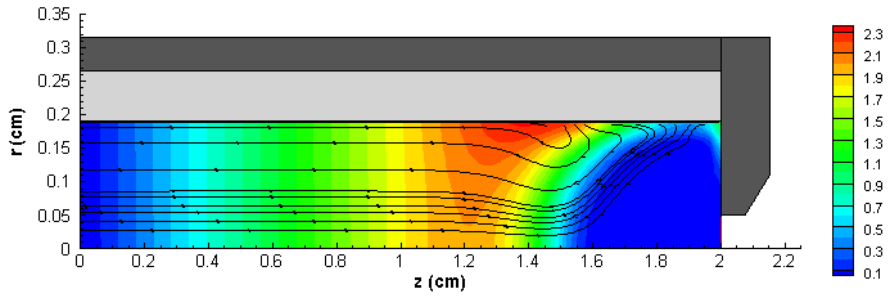

(c) Barium neutral density, $n_{Ba}/10^{16}$ (m^{-3}), for Case 2

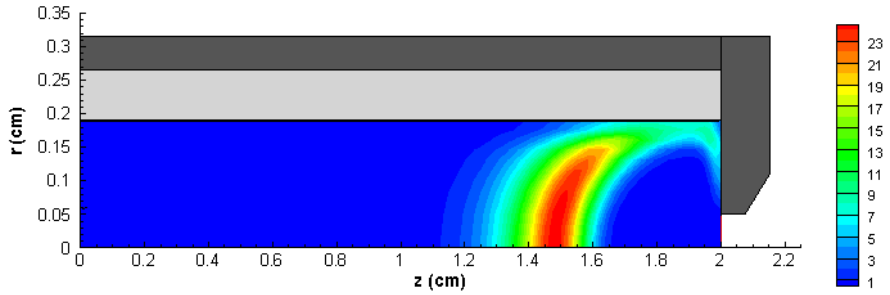

(d) Barium ion density, $n_{Ba+}/10^{14}$ (m^{-3}), for Case 2

Figure 13. Barium neutral and ion density distributions. Streamlines on neutral density plots represent total barium flux (the sum of ion and neutral fluxes).

rate of change of barium atom density on the surface can be expressed as

$$N_0 \frac{\partial \theta}{\partial t} = (\Gamma_{Ba} + \Gamma_{Ba^+})(1-\theta) - \Gamma_d. \tag{16}$$

In this expression, $N_0 = 5 \times 10^{18}$ m^{-2}s^{-1} is the number density of adsorption sites for barium on tungsten,[24] θ is the coverage, or fraction of these sites that are occupied, and $\Gamma_{Ba} = n_{Ba} u_{t,Ba}$ is the flux of barium atoms to the surface at the thermal velocity $u_{t,Ba}$. $\Gamma_{Ba^+} = n_{Ba+} u_B$ is the flux of ions, which enter the cathode sheath at the Bohm velocity $u_B = \sqrt{kT_e/m_{Ba}}$. The sticking coefficient of barium on tungsten is assumed to be unity, so the probability that impinging barium particles will adsorb is proportional to the fraction of open adsorption sites, $(1-\theta)$.

Γ_d is the barium desorption rate from the adsorbed layer. In general this can be described by an Arrhenius-type relationship, $\Gamma_d(T_c, \theta) = N_0 \nu_d(\theta) \exp(E_d(\theta)/kT_c)$, but the desorption energy E_d and pre-exponential factor ν_d are both strong functions of the coverage θ because of adatom interactions. At high values of θ, interactions between neighboring adatoms reduce the binding forces, making it easier for adatoms to thermally desorb. This can be modeled semi-empirically assuming a constant desorption energy and a pre-exponential factor that varies as θ^5. Using desorption data for barium on oxidized tungsten,[24] an expression for the desorption flux in this form can be derived,

$$\Gamma_d = 1.05 \times 10^{25} \theta^5 \exp(-2.06/kT_c). \tag{17}$$

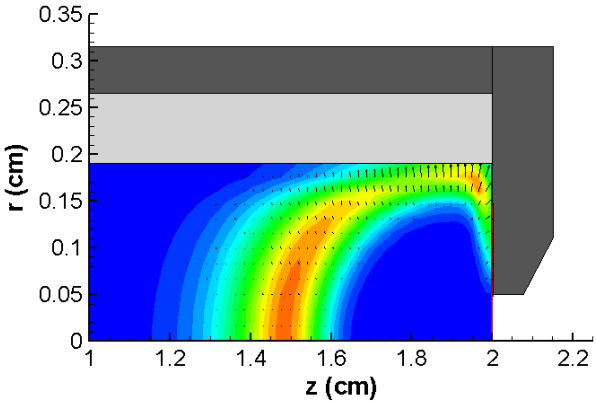

(a) Ion density, $n_{Ba}/10^{14}$ (m^{-3}), and ion flux vectors, Case 1

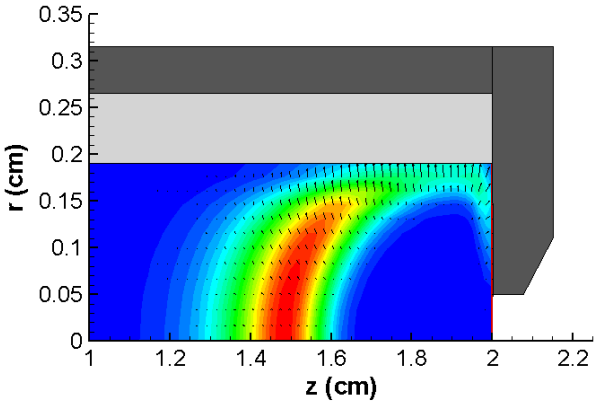

(b) Ion density, $n_{Ba}/10^{14}$ (m^{-3}), and ion flux vectors, Case 2

Figure 14. Barium ion density distributions and ion flux vectors.

Under steady state conditions, the equilibrium surface coverage is given by a balance between the supply rate from the gas phase and loss by desorption,

$$\frac{1-\theta}{\theta^5} = \frac{1.05 \times 10^{25} \exp(-2.06/kT_c)}{n_{Ba} u_{t,Ba} + n_{Ba+} u_B}. \tag{18}$$

For the conditions described here, the ion flux to the emitter is much higher than the neutral flux. The surface coverage corresponding to the calculated ion flux for the measured insert temperature distribution is plotted in Fig. (16). For case 1, the ion flux is so high at the downstream end that the coverage is close to 1. This is a conservative calculation, because it ignores the contribution from surface diffusion out of the pores. For case 2, there is no contribution from the pores in this region, and even though the ion flux is an order of magnitude lower, the coverage is still greater than 0.65 in the electron emission zone. This coverage is comparable to what is maintained in vacuum cathodes by pore flow alone.[24] The coverage values for these two cases are not very different despite large differences in the ion flux because of the strong dependence of the desorption flux on coverage.

The results of simulations for case 2 with operating times of 1000, 10000 and 30000 hours are plotted in Fig. (17). Figure (17a) shows that the neutral barium pressure drops as the net barium flow from the insert is reduced by depletion (greater flow resistance as the reaction front recedes into the insert). The region over which barium can be produced broadens slightly as the barium partial pressure drops relative to the equilibrium vapor pressure, which is constant in this series of simulations because the cathode temperature is held constant. This broadening compensates to some extent for the barium depletion–more of the insert surface can supply barium as the production rate drops.

Figure (17b) demonstrates again that the surface coverage is relatively insensitive to changes in ion flux. The ion flux drops almost a factor of two, roughly in proportion to the decreases in net barium flow and neutral pressure, but the surface coverage drops only about 10%. The coverage levels even after 30000 hours of operation with no barium supply under the electron emission zone are still adequate to maintain high current densities.

IV. Conclusions

The insert analyses and modeling resulted in three main conclusions that have significant implications for hollow cathode lifetime. First, tungsten erosion and subsequent redeposition in the emission zone results in the formation of a dense tungsten shell with reduced porosity. This deposit inhibits barium flow from the interior and therefore suppresses the reaction, resulting in very little barium depletion under the primary electron emission zone. Despite this, hollow cathodes appear to function correctly for very long lifetimes.

The barium transport model shows that barium in the downstream region can be very effectively supplied through the gas phase and will maintain adequate surface coverage in the emission zone for lifetimes on the order of those achieved in long duration tests. The key difference between hollow cathode gas discharges and vacuum dispenser cathodes is that hollow cathodes make much more efficient use of the barium supplied by the insert. Neutral barium from the insert is ionized in the intense xenon plasma, and the combination of the electric field and the drag from the xenon ion flow results in a high barium ion flux to the emitter surface. The ions are neutralized on the surface and return to the discharge to be ionized again. Because the upstream boundary is the only effective sink for barium (except under conditions in which barium can accumulate on the cathode surface; in the presence of oxidizing impurities for instance) a high barium partial pressure builds up at the downstream end.

The high barium partial pressure appears to suppress impregnate reduction reactions over most of the insert length. Barium is evidently supplied only from a narrow region where ionization reduces the neutral density below the equilibrium vapor pressure. This result is the most surprising, and perhaps the most uncertain because it relies on the relative values of thermochemical properties which are not well known. A careful examination of the depletion profile along hollow cathodes from long duration wear tests could help confirm this conclusion. This is another example of self-regulation in hollow cathodes–the barium production rate increases until the pressure builds up sufficiently to suppress reactions over some length of the insert. This suggests that barium located upstream of the electron emission site is not wasted, but is critical to the

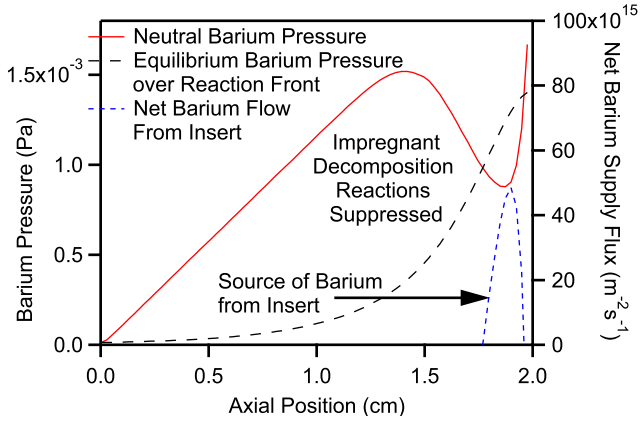

(a) Case 1: Entire insert allowed to emit barium.

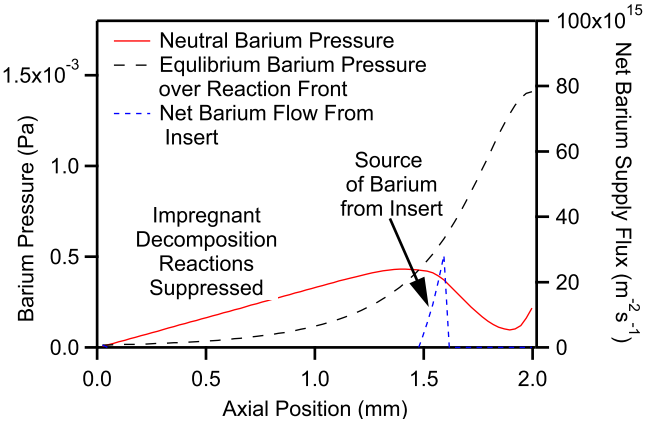

(b) Case 2: Barium emission inhibited in first 4 mm.

Figure 15. Axial distributions of neutral barium pressure, equilibrium vapor pressure and net barium supply rate from the insert interior.

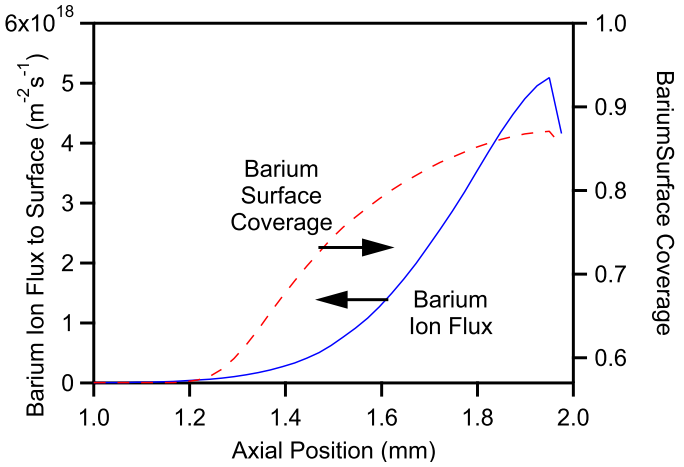

(a) Case 1: Entire insert allowed to emit barium.

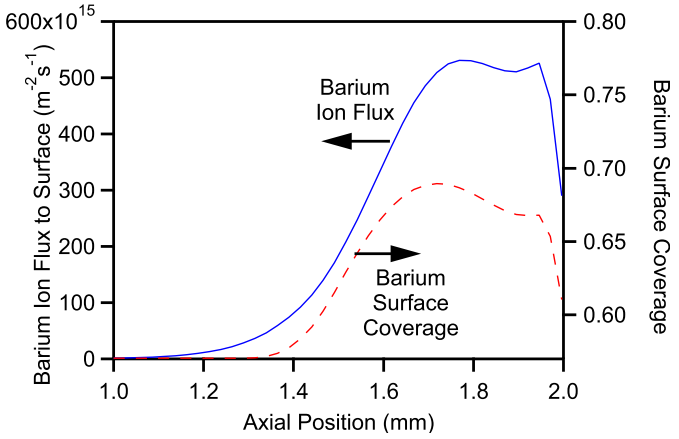

(b) Case 2: Barium emission inhibited in first 4 mm.

Figure 16. Axial distributions of barium ion flux and barium surface coverage.

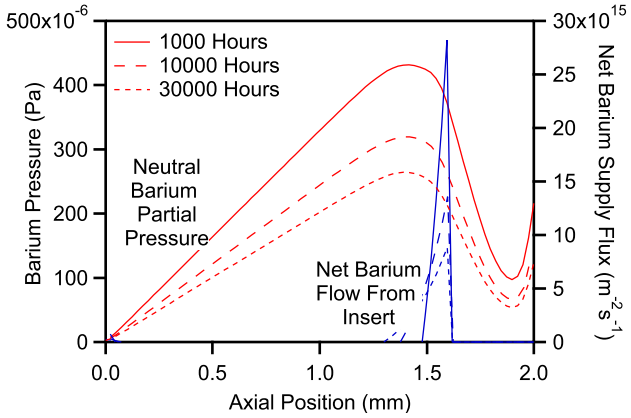

(a) Net barium flow from the insert and resulting neutral barium pressure as a function of operating time

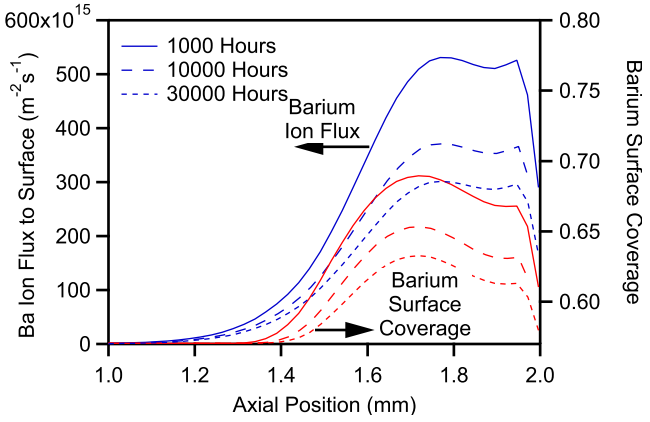

(b) Barium ion flux and equilbrium surface coverage as a function of operating time.

Figure 17. The effect of barium depletion over time on the internal barium gas properties and surface coverage for case 2 (no barium flow through 4 mm length at the downstream end.

operation of the discharge through gas phase resupply and in fact, much of this supply is saved until it is needed. These improvements in understanding of barium transport processes indicate that models of cathode failure due to barium depletion that are based on vacuum dispenser cathode data are likely to be extremely conservative.

V. Acknowledgments

The authors would like to thank Al Owens, Ray Swindlehurst and Ron Watkins for their assistance in preparing the test facility and Ron Ruiz and Jim Kulleck for their contributions in electron microscopy. The research described in this paper was carried out by the Jet Propulsion Laboratory, California Institute of Technology, under a contract with the National Aeronautics and Space Administration.

References

[1]Oh, D., "Evaluation of Solar Electric Propulsion Technologies for Discovery Class Missions," 41^{st} *Joint Propulsion Conference*, Sacramento, CA, 2006, AIAA-2006-4270.

[2]Shroff, A., Palluel, P., and Tonnerre, J., "Performance and Life Tests of Various Types of Impregnated Cathodes," *Applications of Surface Science*, Vol. 8, 1981, pp. 36–499.

[3]Polk, J., Anderson, J., Brophy, J., Rawlin, V., Patterson, M., and Sovey, J., "The Results of an 8200 Hour Wear Test of the NSTAR Ion Thruster," 35^{th} *Joint Propulsion Conference*, Los Angeles, CA, 1999, AIAA-99-2446.

[4]Sengupta, A., Brophy, J., and Goodfellow, K., "Status of the Extended Life Test of the DS1 Flight Spare Ion Engine after 30,352 Hours of Operation," 40^{th} *Joint Propulsion Conference*, Fort Lauderdale, FL, 2004, AIAA-2004-4558.

[5]Sengupta, A., "Destructive Physical Analysis of Hollow Cathodes from the Deep Space 1 Flight Spare Ion Engine 30,000 Hr Life Test," 29^{th} *International Electric Propulsion Conference*, Princeton, NJ, 2005, IEPC 2005-026.

[6]Mikellides, I., Katz, I., Goebel, D., and Jameson, K., "Driving Processes in the Orifice and Near-Plume Regions of a Hollow Cathode," 41^{st} *Joint Propulsion Conference*, Sacramento, CA, 2006, AIAA-2006-5151.

[7]Jameson, K., Goebel, D., Mikellides, I., and Watkins, R., "Local Neutral Density and Plasma Parameter Measurements in a Hollow Cathode Plume," 41^{st} *Joint Propulsion Conference*, Sacramento, CA, 2006, AIAA-2006-4490.

[8]Polk, J., "The Effect of Reactive Gases on Hollow Cathode Operation," 41^{st} *Joint Propulsion Conference*, Sacramento, CA, 2006, AIAA-2006-5153.

[9]Polk, J., "Long and Short Term Effects of Oxygen Exposure on Hollow Cathode Operation," 42^{nd} *Joint Propulsion Conference*, Cincinnati, OH, 2007, AIAA-2007-5191.

[10]Capece, A., Polk, J., and Shepherd, J., "Surface Characterization of Barium Tungstate Formation in Hollow Cathodes," *Space Propulsion 2008 Conference*, Heraklion, Greece, 2008.

[11]Sarver-Verhey, T., "Destructive Evaluation of a Xenon Hollow Cathode After a 28,000 Hour Life Test," 34^{rd} *Joint Propulsion Conference*, Cleveland, OH, 1998, AIAA-98-3482.

[12]Verhey, T., "Microanalysis of Extended-Test Xenon Hollow Cathodes," 27^{th} *Joint Propulsion Conference*, Sacramento, CA, 1991, AIAA-91-2123.

[13]Brophy, J., "NASA's Deep Space 1 Ion Engine," *Rev. Sci. Inst.*, Vol. 73, No. 2, 2002.

[14]Polk, J., Brinza, D., Kakuda, R., Brophy, J., Katz, I., Anderson, J., Rawlin, V., Patterson, M., Sovey, J., and Hamley, J., "Demonstration of the NSTAR Ion Propulsion System on the Deep Space One Mission," 27^{th} *International Electric Propulsion Conference*, Pasadena, CA, 2001, IEPC-01-075.

[15]Rudwan, I., Wallace, N., Coletti, M., and Gabriel, S. B., "Emitter Depletion Measurement and Modeling in the T5 and T6 Kaufman-type Ion Thrusters," 30^{th} *International Electric Propulsion Conference*, Florence, Italy, 2007, IEPC 2007-256.

[16]Gaertner, G., Geittner, P., Raasch, D., and Wiechert, D., "Supply and Loss Mechanisms of Ba Dispenser Cathodes," *Applied Surface Science*, Vol. 146, 1999, pp. 22–30.

[17]Walker, T. G., Bonin, K., and Happer, W., "Modulation Technique for Measuring Diffusion Coefficients of Ba in Noble Gases," *J. Chem. Phys.*, Vol. 87, 1987, pp. 660–663.

[18]Dettmann, J. and Karstensen, F., "Absolute Ionisation Functions for Electron Impact with Barium," *J. Phys. B: At. Mol. Phys.*, Vol. 15, 1982, pp. 287–300.

[19]Rittner, E., Rutledge, W., and Ahlert, R., "On the Mechanism of Operation of the Barium Aluminate Dispenser Cathode," *J. Appl. Phys.*, Vol. 28, No. 12, 1957, pp. 1468–1473.

[20]Palluel, P. and Schroff, A., "Experimental Study of Impregnated Cathode Behavior, Emission and Life," *J. Appl. Phys.*, Vol. 51, No. 5, 1980, pp. 2894–2902.

[21]Mikellides, I., Katz, I., Goebel, D., and Polk, J., "Hollow Cathode Theory and Experiment. II. A Two-Dimensional Theoretical Model of the Emitter Region," *J. Appl. Phys.*, Vol. 98, 2005, pp. 113303.

[22]Mikellides, I., Katz, I., Goebel, D., and Polk, J., "Theoretical Model of a Hollow Cathode Plasma for the Assessment of Insert and Keeper Lifetimes ," 41^{st} *Joint Propulsion Conference*, Tucson, AZ, 2005, AIAA-2005-4234.

[23]Mikellides, I., Katz, I., Goebel, D., Polk, J., and Jameson, K., "Plasma Processes inside Dispenser Hollow Cathodes," *Phys. Plasmas*, Vol. 13, 2006, pp. 06354.

[24]Forman, R., "Surface studies of barium and barium oxide on tungsten and its application to understanding the mechanism of operation of an impregnated tungsten cathode," *J. Appl. Phys.*, Vol. 47, 1976, pp. 5272–5279.